RCS Estimation of 3D Metallic Targets Using the Moment Method and Rao-Wilton-Glisson Basis Functions

G. K. Carvajal, D. J. Duque, and A. J. Zozaya

Electronics and Communications Department, Applied Electromagnetics Lab.
Carabobo University, Valencia, Venzuela
azozaya@uc.edu.ve

Abstract – This work deals on the estimation of the radar cross section (RCS) of five three-dimensional conductive objects: the metallic sphere, NASA almond, single ogive, double ogive and conesphere, using the Moment Method. The Rao-Wilton-Glisson (RWG) basis functions were used to expand the surface current of targets inside the Electric Field Integral Equation (EFIE). Triangular domains of RWG basis functions were constructed using MATLAB tessellation capabilities and a MATLAB code was developed and run to solve the electromagnetic scattering problem. As a result five RCS graphs, one for each target, were obtained. The accuracy of the program was validated by comparing the obtained results with those reported in the Literature.

Keywords: Radar Cross Section (RCS), Method of Moments (MoM), Electric Field Integral Equation (EFIE), Rao-Wilton-Glisson (RWG) basis functions, and Computational Electromagnetics (CEM).

I. INTRODUCTION

It is well known that the problem of *Electromagnetic Scattering* for targets of arbitrary shape is either difficult or impossible to treat analytically. This is due among others to the complicated effect of targets curvatures, corners, and dielectrics which could overlap the target. This is the reason why in order to get an inside into the scattering mechanism, available numerical methods must be used.

This work deals on the estimation of the radar cross section (RCS) of five three-dimensional conductive objects: the metallic sphere, NASA almond, single ogive, double ogive and conesphere, using the moment method [1]. Most of this objects are radar benchmark targets widely used for the validation of computational electromagnetic codes. Theirs geometries are well described in [2].

The electric current and charge densities at the target surface are expanded using the Rao-Wilton-Glisson (RWG) basis functions [3]. Discretization of target surface is achieved using MATLAB tessellation capabilities taking into account the work of Makarov [4]. Although the MATLAB built-in functions are used for writing the code and for rendering the results, this paper emphasizes the main equations but not on transcribing the code.

This article is organized in the following way: Section 2 presents the theoretical concepts used for the problem. Section 3 presents the numerical approach used to obtain a solution for the scattering problem of electrical conductive objects using the MoM and the RWG basis function. In Section 4 the numerical results obtained from simulation are presented and, finally, in Section 5 conclusions are given.

II. THEORETICAL CONCEPTS

A. The Radar Cross Section

The radar cross section (RCS) is a figure of merit that quantifies the amount of electromagnetic energy scattered in a given direction. The RCS, denoted by the greek letter σ is defined as follow [5,6],

$$\sigma\left(\boldsymbol{\kappa}^{\boldsymbol{i}}, \boldsymbol{\kappa}^{\boldsymbol{s}}\right) = \lim_{r\to\infty}\left(4\pi r^2 \frac{|\boldsymbol{E}^{\boldsymbol{s}}|^2}{|\boldsymbol{E}^{\boldsymbol{i}}|^2}\right) \tag{1}$$

where $\boldsymbol{E}^{\boldsymbol{i}}$ is the incident field in a direction $\boldsymbol{\kappa}^{\boldsymbol{i}}$, $\boldsymbol{E}^{\boldsymbol{s}}$ is the scattered field in a direction $\boldsymbol{\kappa}^{\boldsymbol{s}}$. Whether the directions $\boldsymbol{\kappa}^{\boldsymbol{i}}$ and $\boldsymbol{\kappa}^{\boldsymbol{s}}$ coincide or not, we talk about monostatic RCS or bistatic RCS, respectively. In the present work we will focus on the monostatic RCS, even though the bistatic RCS can also be computed easily.

B. The Electric Field Integral Equation

In *free space*, where a scatterer could be in the presence of a forced incident electric field $\boldsymbol{E}^{\boldsymbol{i}}$, there will be a resultant electric field $\boldsymbol{E}$, given by $\boldsymbol{E} = \boldsymbol{E}^{\boldsymbol{i}} + \boldsymbol{E}^{\boldsymbol{s}}$. In this assumption, the field $\boldsymbol{E}^{\boldsymbol{s}}$ would be the scattered field. Over a Perfect Electric Conductor (PEC) scatterer surface, the tangential component of the electric field must vanish, hence,

$$\boldsymbol{n} \times \left(\boldsymbol{E}^{\boldsymbol{i}} + \boldsymbol{E}^{\boldsymbol{s}}\right) = 0 \tag{2}$$

where $\boldsymbol{n}$ is the scatterer's surface normal vector. The *Equivalence Principle* [5] establishes as a sources for $\boldsymbol{E}^{\boldsymbol{s}}$, a current density $\boldsymbol{J}_{\boldsymbol{s}}$ and a superficial density of charges ρ_s, both related through the *continuity* of current

$\rho_s = -\frac{\nabla\cdot \boldsymbol{J_s}}{\jmath\omega}$. Hence, the $\boldsymbol{E_s}$ could be computed by the following expression,

$$\boldsymbol{E_s} = -\jmath\omega \boldsymbol{A} - \nabla \boldsymbol{V} \tag{3}$$

with

$$\boldsymbol{A}(\boldsymbol{r}) = \frac{\mu}{4\pi}\int_{S'} \boldsymbol{J_s}(\boldsymbol{r'}) G(r,r')\mathrm{d}S',$$
$$V(r) = \frac{1}{4\pi\epsilon}\int_{S'} \rho_s(r') G(r,r')\mathrm{d}S',$$

where $G(r,r') = \frac{e^{-\jmath\kappa|\boldsymbol{r}-\boldsymbol{r'}|}}{|\boldsymbol{r}-\boldsymbol{r'}|}$, $\boldsymbol{r}$ and $\boldsymbol{r'}$ are the position vectors for observation and source points respectively, $\kappa = \omega\sqrt{\mu\epsilon}$ is the wavenumber, and finally S' is the scatterer's surface seen as a source domain. By means of simple substitutions, and taking into account that $-\jmath\omega\rho = \nabla'\cdot \boldsymbol{J}$, equation (2) is rewritten as follows,

$$\boldsymbol{n}\times \jmath\frac{\omega\mu}{4\pi}\int_{S'}\left[\boldsymbol{J_s}(\boldsymbol{r'})G(r,r') + \frac{1}{\kappa^2}\nabla\nabla'\cdot \boldsymbol{J_s}(\boldsymbol{r'})G(r,r')\right]\mathrm{d}s' = \boldsymbol{n}\times\boldsymbol{E_i}. \tag{4}$$

The equation (4) is a integral equation of first kind [7] in the form $\mathcal{L}(\boldsymbol{u}) = \boldsymbol{v}$ known as the electric field integral equation (EFIE), where one recognizes,

$$\mathcal{L}(\,) \equiv$$
$$\boldsymbol{n}\times \jmath\frac{\omega\mu}{4\pi}\int_{S'}\left[(\,)G(r,r') + \frac{1}{\kappa^2}\nabla\nabla'\cdot(\,)G(r,r')\right]\mathrm{d}s'$$
$$\boldsymbol{u} \equiv \boldsymbol{J_s}$$
$$\boldsymbol{v} \equiv \boldsymbol{n}\times\boldsymbol{E_i}.$$

For most of practical targets, equation (4) can not be solved analytically, but must be solved numerically. Equation (4), in principle, will be used to compute the induced current on the PEC scatterer surface.

III. THE NUMERICAL SOLUTION

The numerical solution to equation (4) will be obtained using the moment method as described in [1] . The RWG basis function $\boldsymbol{f_n}$ will be used for the expansion of the induced current $\boldsymbol{J_s}$ [3].

A. Filling the impedance matrix

To fill the impedance matrix Z, two integrals: the integral of the inner product definition $Z_{mn} = \langle \boldsymbol{w_m}, \mathcal{L}(\boldsymbol{f_n})\rangle = \int_{S_m} \boldsymbol{w_m}\cdot\mathcal{L}(\boldsymbol{f_n})$ and the convolution integral given by $\mathcal{L}(\boldsymbol{f_n})$ must be solved $N\times N$ times [1]. The complexity of the former will be determined by the election of the *weighting* function $\boldsymbol{w_m}$. The weighting functions $\boldsymbol{w_m}$ must be in the rank of $\mathcal{L}$ preferably, to accelerate the convergence [1]. Nevertheless, this premise is not restrictive [8]. Although there exist several possibilities for the choosing of $\boldsymbol{w_m}$, in this work it is preferred to use Galerkin approach as Rao et al. [3] suggested.

1) Numerical Integration: The integral $Z_{mn} = \int_{S_m}\boldsymbol{f_m}\cdot\mathcal{L}(\boldsymbol{f_n})\,\mathrm{d}S_m$ will be approximated by the product of its argument evaluated at the barycenter (center of mass) of each triangle and their areas respectively. Hence,

$$Z_{mn} = \int_{T_m^+}\boldsymbol{f_m}\cdot\mathcal{L}(\boldsymbol{f_n})\,\mathrm{d}S + \int_{T_m^-}\boldsymbol{f_m}\cdot\mathcal{L}(\boldsymbol{f_n})\,\mathrm{d}S \tag{5}$$
$$\approx \frac{l_m}{2}\left[\boldsymbol{\rho_m^{c+}}\cdot\mathcal{L}(\boldsymbol{f_n})\big|_{\boldsymbol{\rho_m^{c+}}} + \boldsymbol{\rho_m^{c-}}\cdot\mathcal{L}(\boldsymbol{f_n})\big|_{\boldsymbol{\rho_m^{c+}}}\right]$$

where $\boldsymbol{\rho_m^{c\pm}}$ is the position vector for the barycenters of triangles $T_m^{\pm}$ and l_m is the length of the common edge. Taking into account the definition for $\mathcal{L}$, equation (5) is written as,

$$Z_{mn} = \jmath\omega l_m\left(\boldsymbol{A_{m^+,n}}\cdot\frac{\boldsymbol{\rho_m^{c+}}}{2} + \boldsymbol{A_{m^-,n}}\cdot\frac{\boldsymbol{\rho_m^{c-}}}{2}\right) + l_m\left(V_{m^-,n} - V_{m^+,n}\right) \tag{6}$$

where

$$\boldsymbol{A_{m^\pm,n}} = \frac{\mu}{4\pi}\int_{S'}\boldsymbol{f_n}\frac{e^{-\jmath\kappa R_m^\pm}}{R_m^\pm}\mathrm{d}S',$$

$$V_{m^\pm,n} = -\frac{1}{4\pi\jmath\omega\epsilon}\int_{S'}\nabla'\cdot\boldsymbol{f_n}\frac{e^{-\jmath\kappa R_m^\pm}}{R_m^\pm}\mathrm{d}S',$$

and $R_m^\pm = \left|\boldsymbol{r_m^{c\pm}} - \boldsymbol{r'}\right|$.

Finally, developing equation (6) is obtained for Z_{mn},

$$Z_{mn} = \frac{l_m}{8}\left(\frac{\jmath\eta\kappa}{\pi}\right)\boldsymbol{\rho_m^{c\pm}}\cdot\int_{T_n^+ + T_n^-}\boldsymbol{f_n}G\left(\boldsymbol{r_m^{c\pm}},\boldsymbol{r'}\right)\mathrm{d}S' \pm \frac{l_m l_n}{4}\left(\frac{\jmath\eta}{\pi\kappa}\right)\Big[\frac{1}{A_n^+}\int_{T_n^+}G\left(\boldsymbol{r_m^{c\pm}},\boldsymbol{r'}\right) - \frac{1}{A_n^-}\int_{T_n^-}G\left(\boldsymbol{r_m^{c\pm}},\boldsymbol{r'}\right)\Big] \tag{7}$$

where $\boldsymbol{\rho_m^{c\pm}}$ and $\boldsymbol{r_m^{c\pm}}$ are position vectors for the barycenters of triangles $T_m^\pm$ measured locally and globally, respectively.

To solve the remaining integrals in equation (7), several approaches can be followed [9,10]. Particulary, for this work, it has been adopted to use the so call *barycentric subdivision* [4,11]. According to this, any triangle T is subdivided in 9 subtriangles applying the $1/3$ rule. Hence, the integrand is considered *constant* in any of the subtriangles. Due to this procedure the singularity of equation (4) is avoided because of subtriangle's midpoints for each source triangles $T_n^\pm$ never coincide with centers of observation triangles $T_m^\pm$. The barycentric subdivision is resumed as,

$$\int_S g(\boldsymbol{r})\mathrm{d}S = \frac{A}{9}\sum_{k=1}^{9} g(\boldsymbol{r_k^c}). \tag{8}$$

Applying equation (8) to equation (7), one obtains,

$$Z_{mn} = \jmath \frac{l_m l_n}{144\pi}\omega\mu \boldsymbol{\rho}_{\boldsymbol{m}}^{\boldsymbol{c}\pm} \cdot \sum_{k=1}^{9} \boldsymbol{\rho}_{\boldsymbol{k}}^{\boldsymbol{c}+} G\left(\boldsymbol{r}_{\boldsymbol{m}}^{\pm}, \boldsymbol{r}_{\boldsymbol{k}}^{\boldsymbol{c}+}\right) + \boldsymbol{\rho}_{\boldsymbol{k}}^{\boldsymbol{c}-} G\left(\boldsymbol{r}_{\boldsymbol{m}}^{\pm}, \boldsymbol{r}_{\boldsymbol{k}}^{\boldsymbol{c}-}\right) \pm \jmath \frac{l_m l_n}{36\pi}\frac{1}{\omega\epsilon}\sum_{k=1}^{9} G\left(\boldsymbol{r}_{\boldsymbol{m}}^{\pm}, \boldsymbol{r}_{\boldsymbol{k}}^{\boldsymbol{c}+}\right) - G\left(\boldsymbol{r}_{\boldsymbol{m}}^{\pm}, \boldsymbol{r}_{\boldsymbol{k}}^{\boldsymbol{c}-}\right). \quad (9)$$

Equation (9) shows that $Z_{mn} \equiv Z_{mn^+} + Z_{mn^-}$. Both terms defined in the following way,

$$Z_{mn^+} = \jmath \frac{l_m l_n}{144\pi}\omega\mu \sum_{k=1}^{9} \boldsymbol{\rho}_{\boldsymbol{m}}^{\boldsymbol{c}\pm} \cdot \boldsymbol{\rho}_{\boldsymbol{k}}^{\boldsymbol{c}+} g_m^{\pm}\left(\boldsymbol{r}_{\boldsymbol{k}}^{\boldsymbol{c}+}\right) \pm \jmath \frac{l_m l_n}{36\pi}\frac{1}{\omega\epsilon}\sum_{k=1}^{9} g_m^{\pm}\left(\boldsymbol{r}_{\boldsymbol{k}}^{\boldsymbol{c}+}\right) \quad (10a)$$

$$Z_{mn^-} = \jmath \frac{l_m l_n}{144\pi}\omega\mu \sum_{k=1}^{9} \boldsymbol{\rho}_{\boldsymbol{m}}^{\boldsymbol{c}\pm} \cdot \boldsymbol{\rho}_{\boldsymbol{k}}^{\boldsymbol{c}-} g_m^{\pm}\left(\boldsymbol{r}_{\boldsymbol{k}}^{\boldsymbol{c}-}\right) \pm \jmath \frac{l_m l_n}{36\pi}\frac{1}{\omega\epsilon}\sum_{k=1}^{9} g_m^{\pm}\left(\boldsymbol{r}_{\boldsymbol{k}}^{\boldsymbol{c}-}\right), \quad (10b)$$

where $g_m^{\pm}\left(\boldsymbol{r}_{\boldsymbol{k}}^{\boldsymbol{c}\pm}\right) = G\left(\boldsymbol{r}_{\boldsymbol{m}}^{\pm}, \boldsymbol{r}_{\boldsymbol{k}}^{\boldsymbol{c}\pm}\right)$.

Even when the definitions in equation (10) could be trivial, they give the opportunity to fill $[Z]$ using a *triangle-triangle* approach instead of a *edge-edge* approach, making the filling of $[Z]$ faster.

B. Computing the Scattered Field

Once the $\boldsymbol{J_s}$ has been computed through the MoM equation $[Z][I] = [V]$, the scattered field $\boldsymbol{E_s}$ must be determine to estimate the RCS $\sigma\left(\boldsymbol{\kappa^i}, \boldsymbol{\kappa^s}\right)$. The approach used in this work to computed $\boldsymbol{E^s}$ is based on the *dipole approximation* (see Fig. 1) [4].

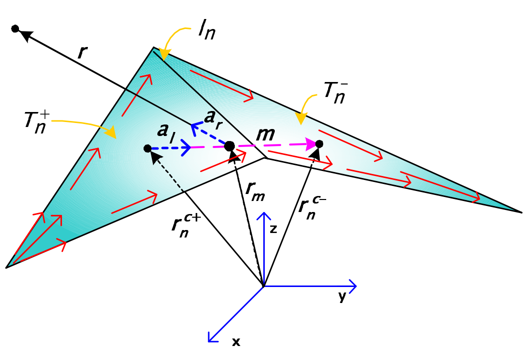

Fig. 1. Equivalent dipole associated with a generic RWG basis function.

This approach states for the particular case that: *The electric field radiated by one single RWG basis function* $\boldsymbol{f_n}$ *can be approximated at far distances by that one of a dipole placed from* $\boldsymbol{r}_{\boldsymbol{n}}^{\boldsymbol{c}+}$ *to* $\boldsymbol{r}_{\boldsymbol{n}}^{\boldsymbol{c}-}$ *with current moment* $\boldsymbol{I\Delta l} = I_n l_n\left(\boldsymbol{r}_{\boldsymbol{n}}^{\boldsymbol{c}-} - \boldsymbol{r}_{\boldsymbol{n}}^{\boldsymbol{c}+}\right)$. Hence, the generalized expression for the $\boldsymbol{E^s}$ would be the following,

$$\boldsymbol{E_s} = \sum_{n=1}^{N} \jmath\kappa\eta \frac{e^{-\jmath\kappa|\boldsymbol{r}-\boldsymbol{r_m}|}}{4\pi|\boldsymbol{r}-\boldsymbol{r_m}|}(\boldsymbol{M}-\boldsymbol{m}) \quad (11)$$

$$\boldsymbol{H_s} = \sum_{n=1}^{N} \jmath\kappa \frac{e^{-\jmath\kappa|\boldsymbol{r}-\boldsymbol{r_m}|}}{4\pi|\boldsymbol{r}-\boldsymbol{r_m}|}(\boldsymbol{m}\times\boldsymbol{a_r}), \quad (12)$$

with $\boldsymbol{M} = (\boldsymbol{r}\cdot\boldsymbol{m})/r^2$, $\boldsymbol{m} = m\boldsymbol{a_l}$ according to Fig. 1 and N is the number of edges in the target discretization.

IV. SIMULATION AND RESULTS

In order to evaluate the method explained in the preceding sections, a total of five targets were chosen. These targets have been extensively used by the electromagnetics community as benchmark targets to validate computational electromagnetic methods. To illuminate them, a plane wave is used as the electromagnetic incident field. The parametric equations that model their surfaces can be found in [2]. The chosen targets are presented in Fig. 2.

Figure 3 represents the RCS computed for the metallic sphere as a function of the frequency. It has been performed a frequency sweep in the range of $0.1 \le \frac{2\pi a}{\lambda} \le 6$ with $a = 1\text{m.}$, the radius of the sphere. In Fig. 3 the computed RCS is plotted in continuos red line, while the benchmark values already reported in [12] are plotted using blue rhombus.

Figure 4 represents the monostatic RCS computed for the metallic almond at 1.19 GHz. It is descomposed in terms of vertical σ_{VV} and horizontal σ_{HH} polarized radar cross section as a function of incident angle ϕ, starting from $0°$ and stoping at $180°$ using $0.125°$ as a step size. The elevation angle is zero. Zero degrees azimuth corresponds to an incident on the tip. At 1.19 GHz the metallic almond is one wavelength long. The incident angle is the azimuth in a standard spherical coordinate system. The σ_{VV} and σ_{HH} are defined when $|\boldsymbol{E_i}| = 1$ as,

$$\sigma_{VV} = \lim_{r\to\infty} 4\pi r^2 \left|\boldsymbol{E_s^V}\right|^2 \quad (13)$$

$$\sigma_{HH} = \lim_{r\to\infty} 4\pi r^2 \left|\boldsymbol{E_s^H}\right|^2. \quad (14)$$

The computed estimations of vertical and horizontal RCS are plotted in blue and red continuos line, while the benchmark reported in [2] is plotted as rhombus and squares, respectively.

Figure 5 represents the monostatic RCS computed for the metallic single ogive at 1.18 GHz. The RCS for both, the vertical and the horizontal are plotted in dBSM, as a function of the azimuth angle. The elevation angle is zero again. Zero degrees azimuth correspond to an incident normal to a tip of the metallic single ogive. As

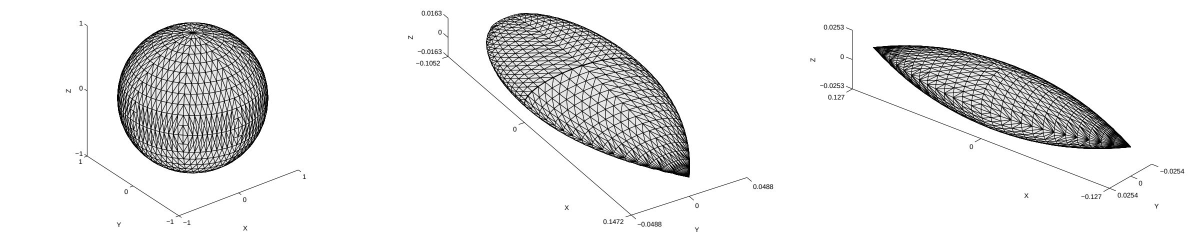

(a) Metallic sphere with 2272 triangles. (b) Metallic almond with 1792 triangles. (c) Metallic single ogive with 1900 triangles.

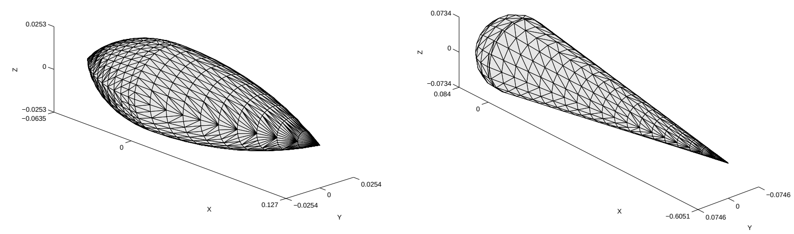

(d) Metallic double ogive with 1520 triangles. (e) Metallic conesphere with 900 triangles.

Fig. 2. Chosen Target to validate the method.

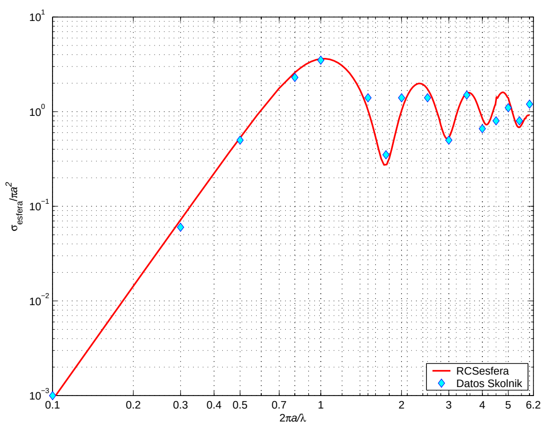

Fig. 3. Estimated RCS for the Metallic Sphere as a function of frequency.

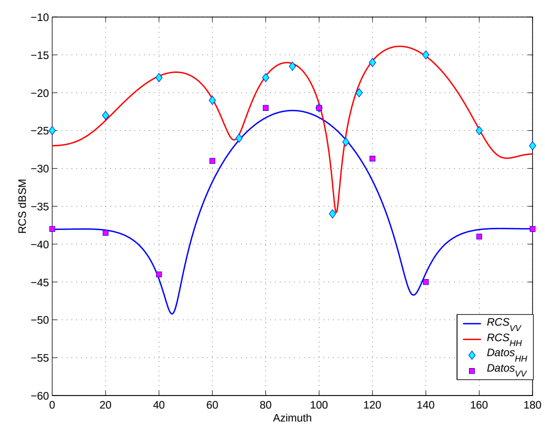

Fig. 4. Estimated σ_{VV} and σ_{HH} for the metallic almond as a function of the incident angle ϕ.

expected, the vertically and horizontally polarized RCS are equal at $0°$ and $180°$ of azimuth in Fig. 5. At 1.18 GHz, the metallic single ogive is one wavelength long. The computed estimations for vertical and horizontal RCS are plotted in blue and red continuos line, respectively, while the benchmark is plotted as rhombus and squares.

Figure 6 represents the monostatic RCS computed for the metallic double ogive at 1.57 GHz. It is decomposed in terms of vertical σ_{VV} and horizontal σ_{HH} polarized radar cross section as a function of incident angle ϕ. The RCS for both the vertical and the horizontal polarized RCS are plotted in dBSM. The elevation angle is zero. At 1.57 GHz the metallic double ogive is one wavelength long.

Figure 7 represents the monostatic RCS computed for the metallic cone-sphere at 869 MHz. Both horizontal and vertical polarizations are plotted against azimuthal angle. Zero degrees azimuth is toward the pointed end. At 869 MHz, this target is two wavelength long. Good agreement between the computed RCS and those used as a reference is observed from the previous figure.

V. CONCLUSIONS

In this work, the Method of Moments (MoM) with Rao-Wilton-Glisson basis functions has been used to develop and test a method for the estimation of the radar cross section for metallic conductive object of arbitrary

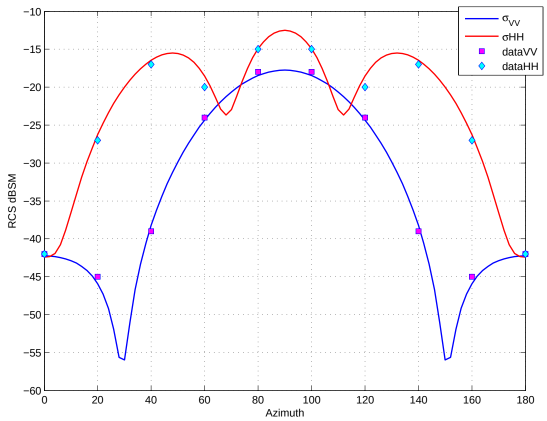

Fig. 5. Estimated σ_{VV} and σ_{HH} for the metallic single ogive as a function of the incident angle ϕ.

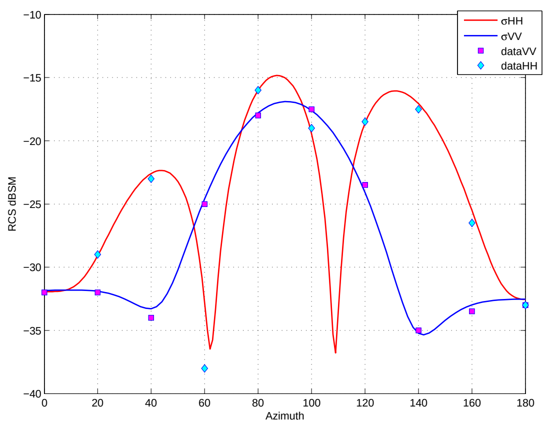

Fig. 6. Estimated σ_{VV} and σ_{HH} for the metallic double ogive as a function of the incident angle ϕ.

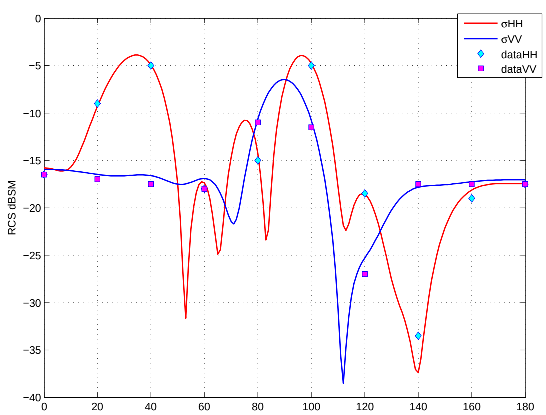

Fig. 7. Estimated σ_{VV} and σ_{HH} for the metallic cone-sphere as a function of the incident angle ϕ.

shape. It has used five extensively used targets to test and validate the method employed. Excellent agreement is seen between the computed results and those already reported in previous investigation. The numerical procedure already described can be easily extended to scatterers of any geometrical shape.

REFERENCES

[1] R. F. Harrington, *Field Computation by Moment Methods*, MacMillan, U.S.A., New York, 1968.

[2] J. L. Volakis, "Benchmark radar targets for the validation of computational electromagnetics programs," *IEEE Antennas and Propagation Magazine*, vol. 35, pp. 84–89, 1993.

[3] S. M. Rao, D. R. Wilton, and A. W. Glisson, "Electromagnetic scattering by surfaces of arbitrary shape," *IEEE Transactions on Antennas and Propagation*, vol. 30, no. 3, pp. 409–418, May 1982.

[4] S. N. Makarov, *Antenna Modeling EM with MATLAB®*, Wiley-Interscienci e, 2002.

[5] R. F. Harrington, *Time-Harmonic Electromagnetics Fields*, McGraw-Hill, U.S.A., 1961.

[6] K. F. Warnick, "Computational electromagnetics course notes," http://www.ee.byu.edu/faculty/warnick/, January 2004.

[7] F. G. Tricomi, *Integral Equations*, Interscience Publishers, Inc., 1957.

[8] T. K. Sarkar, "A note on the choice weighting functions in the method of moments," *IEEE Transactions on Antennas and Propagation*, vol. 33, no. 4, pp. 436–441, April 1985.

[9] J. S. Savage and A. F. Peterson, "Quadrature rules for numerical integration and tetrahedra," *IEEE Antennas and Propagation Magazine*, vol. 38, no. 3, pp. 100–102, June 1996.

[10] R. D. Graglia, "On the numerical integration of the linear shape functions times the 3-d green's function or its gradient on a plane triangle," *IEEE Transactions on Antennas and Propagation*, vol. 41, no. 10, pp. 1448–1455, October 1993.

[11] Y. Kamen and L. Shirman, "Triangle rendering using adaptive subdivision," *IEEE Computer Graphics and Applications*, pp. 95–103, March/April 1998.

[12] M. I. Skolnik, *Introduction to Radar Systems*, McGraw Hill, 1980.

D. J. Duque received his degree in electrical engineering from the University of Carabobo in Venezuela in 2005. In 2007 he completed his M.Sc from both the Universitat Politecnica de Catalunya in Spain and the Politecnico di Torino in Italy. He is currently working toward his PhD in Applied Electromagnetic at the Technische Universiteit Eindhoven in the Netherlands. His research interests include Antenna Design , Electromagnetics Theory and its computational aspects.

G. Carvajal received her degree of Electrical Engineer in 2005 at University of Carabobo (Venezuela). In 2007 she finished her master's studies from the European double degree master program MERIT, at Universitat Politécnica de Catalunya (Spain) and Politècnico di Torino (Italy). Currently she is pursuing the doctoral degree at the Department of Radio and Space Science of Chalmers University of Technology (Sweden). Her principal fields of interests for research include remote sensing and applied electromagnetism.

A. J. Zozaya received the electronic engineering degree from the Polytechnic University of the National Armed Forces (IUPFAN), Maracay, Venezuela, in 1991 and the Doctor degree from the Polytechnic University of Catalonia (UPC), Barcelona, Spain, in 2002. He joined the Electronic and Communication Department of the University of Carabobo, Valencia, Venezuela, in 1994 where he is currently an Associated Professor and the Head of the Applied Electromagnetic Laboratory. His research interests include RF power amplifier linearization techniques and computational electromagnetic.